Contents

Vol. 38, No. 7, 2011
Simultaneous English language translation of the journal is available from Allerton Press, Inc.
Distributed worldwide by Springer. *Bulletin of the Lebedev Physics Institute* ISSN 1068-3356.

ISSN 1068-3356, Bulletin of the Lebedev Physics Institute, 2011, Vol. 38, No. 7, pp. 191–197. © Allerton Press, Inc., 2011.
Original Russian Text © A.M. Galper, S.V. Borisov, V.G. Zverev, C.I. Suchkov, N.P. Topchiev, M.O. Farber, M.I. Fradkin, Yu.T. Yurkin, 2011, published in Kratkie Soobshcheniya po Fizike, 2011, Vol. 38, No. 7, pp. 14–23.

Method for Reconstructing the Gamma-Ray Arrival Direction in the Converter + Calorimeter System

A. M. Galper[a,b], S. V. Borisov[b], V. G. Zverev[b], C. I. Suchkov[a], N. P. Topchiev[a], M. O. Farber[b], M. I. Fradkin[a], and Yu. T. Yurkin[b]

[a] *Lebedev Physical Institute, Russian Academy of Sciences, Leninskii pr. 53, Moscow, 119991 Russia; e-mail: tnp51@rambler.ru*
[b] *National Research Nuclear University "MEPhI", Kashirskoe sh. 31, Moscow, 115409 Russia*

Received January 20, 2011

Abstract—When designing devices of modern gamma astronomy, one of the most important problems is achieving the maximum possible angular resolution. This study is devoted to the method for reconstructing the arrival direction of primary gamma-rays with energies $E_\gamma > 10$ GeV in the GAMMA-400 satellite experiment. By the example of the GAMMA-400 gamma telescope, the possibility of improving the angular resolution of gamma telescopes incorporating a "converter + calorimeter" system is shown. The dependence of the angular resolution on the step of silicon strips used to determine the coordinates of incident particles in the converter and calorimeter and the distance between the converter and calorimeter is analyzed.

DOI: 10.3103/S1068335611070013

Keywords: gamma-telescope, gamma-ray arrival direction.

When designing devices of modern gamma astronomy, one of the most urgent problems is achieving the maximum possible angular resolution. In this case, the gamma-ray detection principle [1–4] often consists in the use of two detector units one of which is a gamma-ray converter and another is a calorimeter. An important problem in designing such experiments is choosing a technique for reconstructing the gamma-ray arrival direction which, for a given configuration, is characterized by the angular resolution. In this paper, we present the method for reconstructing the gamma-ray arrival direction in the GAMMA-400 experiment [5, 6].

The GAMMA-400 gamma telescope is intended to study discrete sources of high-energy gamma radiation (supernovae remnants, pulsars, black holes, molecular clouds, etc.) in the energy range of 0.1–3000 GeV, to measure energy spectra of galactic and extragalactic diffuse gamma radiation, to study gamma-ray bursts coming from space and gamma radiation of the active Sun. A special problem is the study of gamma-ray, electron, and positron fluxes which can be caused by annihilation or decay of dark matter particles.

The GAMMA-400 will be installed at the "Navigator" spacecraft platform. This experiment is performed by the Lebedev Physical Institute of the Russian Academy of Sciences (Moscow) in collaboration with the National Research Nuclear University "MEPhI" (Moscow), National Institute of Nuclear Physics (Italy), All-Russian Research Institute of Electromechanics (Moscow), Institute of High-Energy Physics (Protvino, Moscow oblast), Ioffe Physical Technical Institute (St.Petersburg), and Space Research Institute of the Russian Academy of Sciences (Moscow).

GAMMA-400 gamma telescope is intended to detect gamma-rays, electrons, and positrons with high angular and energy resolution. Some GAMMA-400 parameters and a version of the physical diagram are given in Table 1 and in Fig. 1.

Detection principle. Gamma-rays pass through the anticoincidence segmented scintillation detector AC without interaction and are converted into electron–positron pairs in the converter C. The latter consists of six tungsten layers 0.14 rlu (radiation length units) thick; under each layer, silicon strip (x, y) coordinate detectors CD1–CD6 are arranged with a step of 0.1 mm. C1 and C2 form the time-of-flight system TFS consisting of two scintillation detectors spaced by 100 cm. The silicon strip

Table 1. Expected parameters of the GAMMA-400 gamma telescope

Energy range	100 MeV − 3000 GeV
Sensitive area, cm^2	6400
Sensitivity ($E_\gamma > 100$ MeV), photon/(cm^2 s)	$\sim 2 \times 10^{-9}$
Angular resolution ($E_\gamma > 100$ GeV)	$\sim 0.01°$
Energy resolution ($E_\gamma > 10$ GeV)	$\sim 1\%$
Proton rejection	$\sim 10^6$

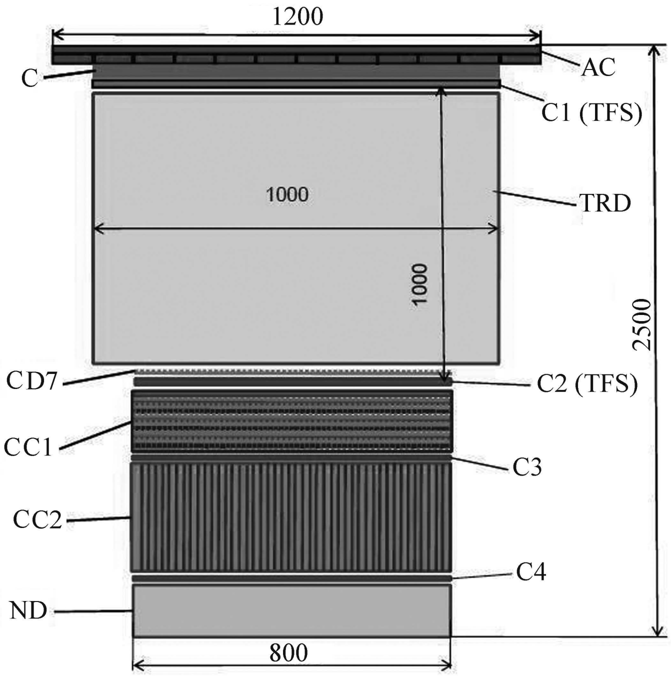

Fig. 1. Physical diagram of the GAMMA-400 gamma telescope. AC is the anticoincidence detector, C is the converter containing six 0.14-rlu layers of tungsten + Si (x, y) strip detectors (step is 0.1 mm), CD7 is the Si (x, y) strip detector (0.1 mm), C1 and C2 are TFS detectors, TRD is the transition radiation detector, CC1 is the position-sensitive calorimeter (10 rlu) with ten layers of Si (x, y) strip detectors (step is 0.5 mm) + BGO (1 rlu), CC2 is the electromagnetic BGO calorimeter (21.5 rlu), C3 and C4 are scintillation detectors, and ND is the neutron detector.

(x, y) coordinate detector CD7 determines points of electron–positron pair (produced by gamma-ray conversion) passage through it with a step of 0.1 mm. Then the electron–positron pair induces an electromagnetic shower in two parts of the coordinate-sensitive calorimeter (CC1 and CC2). The CC1 is an assembly of 10 BGO crystal layers $1 \times 2 \times 40$ cm^3 in size, sandwiched by silicon strip (x, y) coordinate detectors with a step of 0.5 mm. The CC2 is completely assembled from BGO crystals $2 \times 2 \times 40$ cm^3 in size. The CC1 and CC2 thicknesses are 10 and 21.5 rlu, respectively. To determine the number of particles coming from CC1 and CC2, scintillation detectors C3 and C4 are installed. To separate gamma-rays, electrons, and positrons against the background of cosmic ray protons, the transition radiation detector TRD, CC1 and CC2, and neutron detector ND were used. In the two latter cases, this separation was based, respectively, on the difference in the longitudinal and transverse profiles of electromagnetic and hadron showers and the difference in the neutrons produced in the calorimeter traversed by these showers.

A "reverse current" system is used in the gamma telescope, which allows exclusion of AC detector triggering caused by particles moving in the opposite direction from the calorimeter to AC. To exclude "reverse" events, two methods are used, the amplitude–time analysis and AC detector segmentation.

Gamma telescope observations (measurements) are performed using simultaneously two main trigger systems, one for detecting gamma-rays in the absence of AC signals and another for detecting electrons and positrons in the presence of AC signals.

The GAMMA-400 incorporates a system for determining the orientation (star tracker), which allows knowledge of the gamma telescope axis with an accuracy up to 0.005°.

Method for reconstructing the gamma-ray arrival direction. The angular resolution of gamma telescopes reflects the determination accuracy of the arrival direction of detected gamma-rays. At present, due to the insufficient angular resolution of the Fermi-LAT telescope, about half the detected discrete gamma sources remain unidentified [7]. The method planned to be used in the GAMMA-400 experiment provides a significantly better angular resolution in comparison with that of existing and designing telescopes.

To reconstruct the arrival direction of primary gamma-rays, information from silicon strips of CC1 and CD6 planes is used. The reconstruction algorithm includes the following steps.

1. At the first stage, the axis of the shower developed in the CC1 is determined. The axis determination algorithm is described in detail in [8] and was successfully applied to process the PAMELA experiment data [9]. Let us recall the essence of the method.

1.1. For each strip plane, the centroids $\bar{x}_i$ (hereafter, similarly for the y-coordinate) of energy losses are determined by the formula

$$\bar{x}_i = \frac{\sum\limits_j x_{ij} E_j}{\sum\limits_j E_j},$$

where j is the strip number in the plane, E_j is the energy loss in the j-th strip, and $i = 1...10$ are the strip plane numbers. In the first iteration, summation is performed over all plane strips (see 1.3).

1.2. The obtained dependence of $\bar{x}_i$ on the depth z_i (the z axis is perpendicular to the x and y axes) is fitted as a linear function by the least-squares method, i.e., the coefficients of the function

$$\bar{x} = A \cdot z + B \tag{1}$$

(here $z = 0$ corresponds to the $i = 1$ plane) are written as

$$A = \frac{\sum\limits_2^{10} x_i z_i \omega_i - \sum\limits_2^{10} x_i \omega_i \sum\limits_2^{10} z_1 \omega_i}{\sum\limits_2^{10} z_i^2 \omega_i - \left(\sum\limits_2^{10} z_i \omega_i\right)^2}, \tag{2}$$

$$B = \frac{\sum\limits_2^{10} x_i \omega_i \sum\limits_2^{10} z_i^2 \omega_i - \sum\limits_2^{10} z_i \omega_i \sum\limits_2^{10} x_i z_i \omega_i}{\sum\limits_2^{10} z_i^2 \omega_i - \left(\sum\limits_2^{10} z_i \omega_i\right)^2}. \tag{3}$$

As can be seen, planes 2–10 are considered in this case. Such choice is caused by the fact that the shower is sufficiently developed for the energies under consideration in the indicated planes [8].

Here $\omega_i = \frac{E_i}{E_{\rm Ntot}}$ are the weights proportional to the energy release E_i in corresponding planes $(\sum\limits_i \omega_i = 1)$ and $E_{\rm Ntot}$ is the total energy release in the chosen set of planes for reconstructing the shower axis.

1.3. Then the previous two steps are repeated in several iterations; in this case, the centroid $\bar{x}_i$ of this iteration is calculated by summing over strips within the range $\bar{x} \pm r_s$, where $\bar{x}$ was calculated by formula (1) in the previous iteration, and r_s is the parameter defining summation limits in the number of strips. The value of r_s was chosen by optimization results.

Thus, the coefficients A and B (for each x and y projections) specifying the gamma-ray arrival direction according to the CC1 data are determined.

2. In the next stage, information from CD6 planes (x and y) is used.

2.1. The strip $j_{\max}$ with maximum energy release in the range $((A + dA)Z_{CD6} + B, (A - dA)Z_{CD6} + B))$ is determined, where Z_{CD6} is the z-coordinate of CD6 and dA is chosen as 3σ of the calculated distribution over A, obtained based on the results of simulation and processing of these data using algorithm 1.1–1.3. Thus, the number of considered CD6 strips is limited, which decreases the effect of the "reverse current" from the calorimeter on the results obtained.

2.2. Thus, CD6 yields one more point (by coordinates x and y) $\bar{x}_{j\max}$, and the dependence of $\bar{x}$ on z is obtained again (now for ten points), which is fitted by a linear function by the least-squares method, which, as shown below, significantly improves the resolution over A in comparison with item 1. In this case, for current A and B, $\bar{x}$ in CC1 are determined in the similar way as in item 1.3 with the same limiter r_s. The weight W_{CD6} of the point $\bar{x}_{j\max}$ is chosen as $W_{CD6} = \left(\dfrac{ds}{ds_{CD6}}\right)^2 \cdot \dfrac{Z_{CC1}}{Z_{CC1} + H} \cdot \dfrac{1}{N}$, where ds is the step of CC1 strips, ds_{CD6} is the step of CD6 strips, Z_{CC1} is the CC1 thickness ($\sim$15 cm), H is the distance between CD6 and CC1, and $N = 10$ is the number of points for fitting. Here the square of the expression $\left(\dfrac{ds}{ds_{CD6}}\right)$ is caused by the importance of the relative width of CD6 strips from the viewpoint of the contribution to the point weight. Weights of other points are $\omega_i = (1 - W_{CD6})\dfrac{E_i}{E_{\text{Ntot}}}$.

2.3. Then the previous two steps are repeated in several iterations; at the second iteration, dA is decreased by half (this value is chosen proceeding from the calculations performed) in comparison with the first one. In the subsequent several iterations, dA is decreased by 10% in each.

As shown below, the idea to place the converter (and strip detectors) at a distance from the calorimeter provides a significant gain in the angular resolution.

Results. The passage of gamma-ray fluxes of various energies through the GAMMA-400 gamma telescope was simulated in the Geant4.9.2.p03 environment [10]. The simulation results were processed using the program for reconstructing the gamma-ray arrival direction.

Figure 2 shows the distributions of values of A (A is the slope to the z axis) reconstructed only by the CC1 data (Fig. 2(a)) and for the CC1 + CD6 system (Fig. 2(b)) for the vertical gamma-ray flux. Particles are incident on the device center. The gamma-ray energy is 100 GeV. The calculation results are given for the following configuration: $H = 60$ cm, the CD6 strip step is 0.1 mm, the CC1 strip step is 0.5 mm. A comparison of two distributions shows that the additional point near the converter improves the angular resolution by an order of magnitude in this case (the values are given in degrees). In this study, the angular resolution is understood as the root-mean-square deviation of the corresponding distribution over A.

Figure 3 shows the energy dependence of the angular resolution of only CC1 for strip steps of 0.5 and 1.0 mm.

As expected, the angular resolution of CC1 improves as the strip step decreases.

Figure 4 shows the energy dependence of the angular resolution of the CD6 + CC1 system of the GAMMA-400 gamma telescope for various strip steps at the converter–calorimeter distance $H = 60$ cm. Here the parameter $r_s = 10$ for all points, except for the points for the configuration with 0.5 mm for CD6 and CC1, where $r_s = 15$ was chosen for points $E = 250$, 500, 1000 GeV according to results of optimization. Among the considered configurations, the best resolution was obtained at 0.1 and 0.5 mm for CD6 and CC1 strips, respectively.

Figures 5(a) and 5(b) show the dependence of the calculated angular resolution of the GAMMA-400 (for the configuration with 0.1 and 0.5 mm for CD6 and CC1, respectively) on the converter–calorimeter distance for energies of 100 and 1000 GeV, respectively. As expected, the dependences are approximately linear.

Figure 6 shows the energy dependences of the GAMMA-400 angular resolution for the configuration with CD6 and CC1 strip steps of 0.1 and 0.5 mm, respectively, at $H = 60$ and 100 cm.

Thus, for the GAMMA-400 gamma telescope configuration (CD6 and CC1 strip steps are 0.1 and 0.5 mm, respectively, $H = 100$ cm), the angular resolution is better than 0.015° for gamma-ray energies above 100 GeV, which is significantly better than that of existing and designing gamma telescopes.

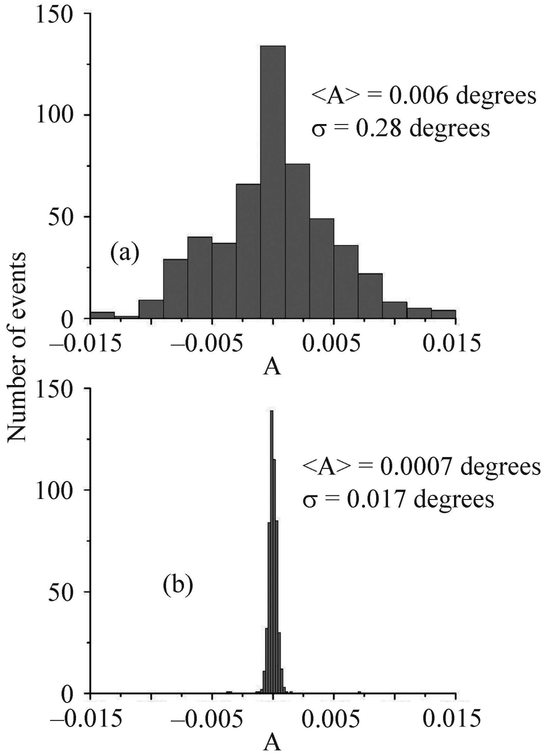

Fig. 2. Distributions of reconstructed values of A (a) only by the CC1 data and (b) by the data of the CC1 + CD6 system.

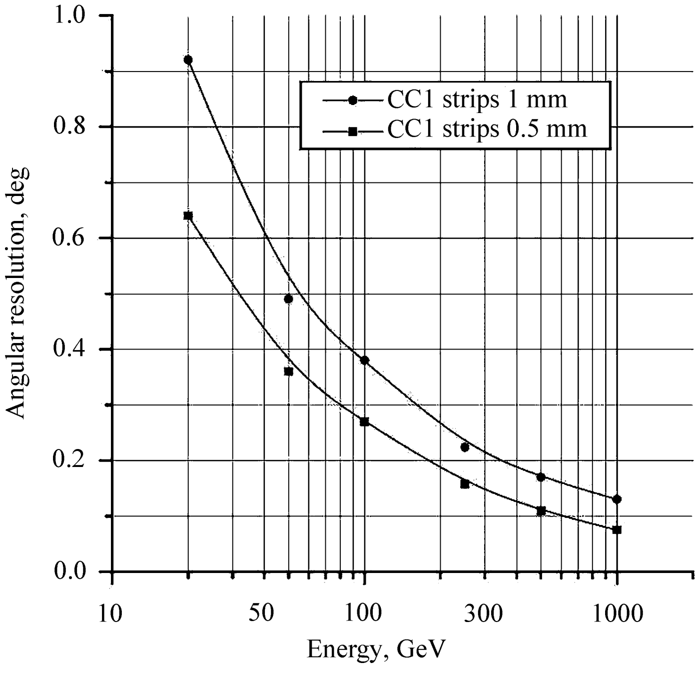

Fig. 3. Energy dependence of the angular resolution of the CC1 system.

In the future, to improve the determination accuracy of the gamma-ray arrival direction of the GAMMA-400, it is planned to additionally use information from CD1–CD5 detectors (which would allow more accurate determination of the gamma-ray conversion point, hence would reduce the role of

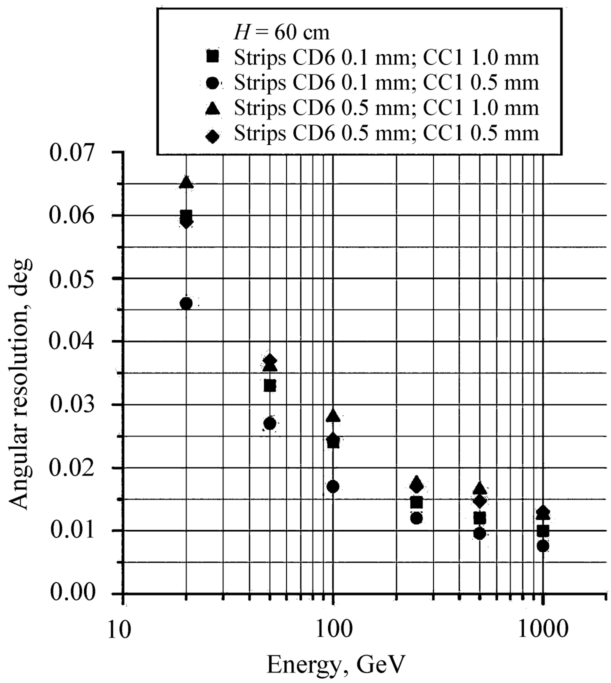

Fig. 4. Energy dependence of the angular resolution of the CD6 + CC1 system of the GAMMA-400 gamma telescope.

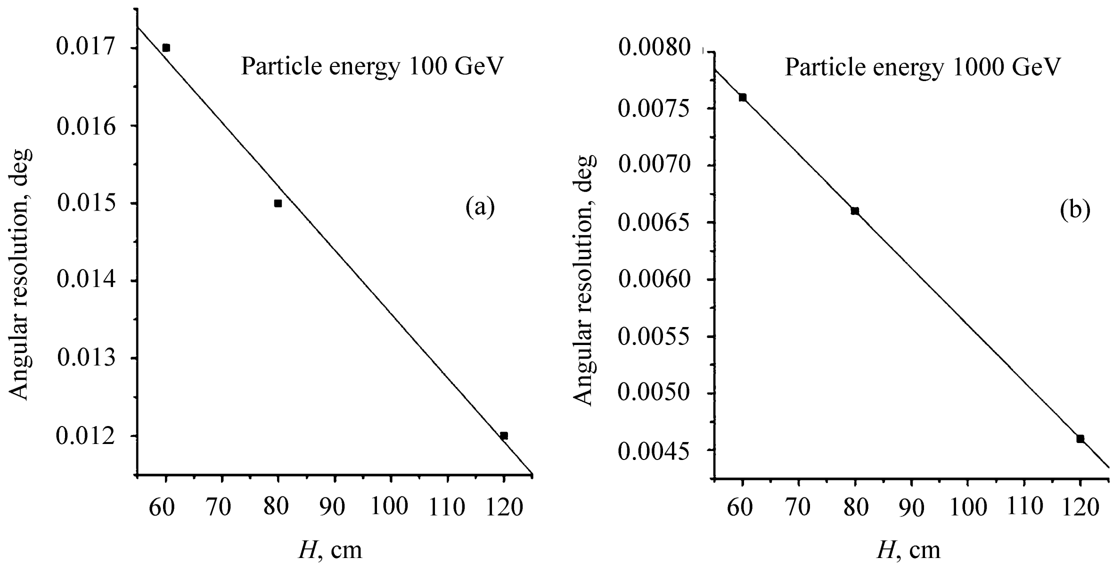

Fig. 5. Dependence of the GAMMA-400 angular resolution on the converter–calorimeter distance H for the particle energy of (a) 100 and (b) 1000 GeV.

multiple scattering in the converter), as well as data from CD7 and BGO detectors. It is also planned to consider the charge distribution over strips at particle passage (which improves the coordinate resolution of detectors).

The determination accuracy of the gamma-ray arrival direction is controlled by both the gamma telescope configuration and the data processing technique. Most modern gamma telescopes incorporate a gamma-ray converter and calorimeter system. In this study, by the example of the GAMMA-400 telescope, the dependence of the angular resolution of the system on the configuration parameters, such as the strip step and the converter–calorimeter distance was demonstrated. The technique for

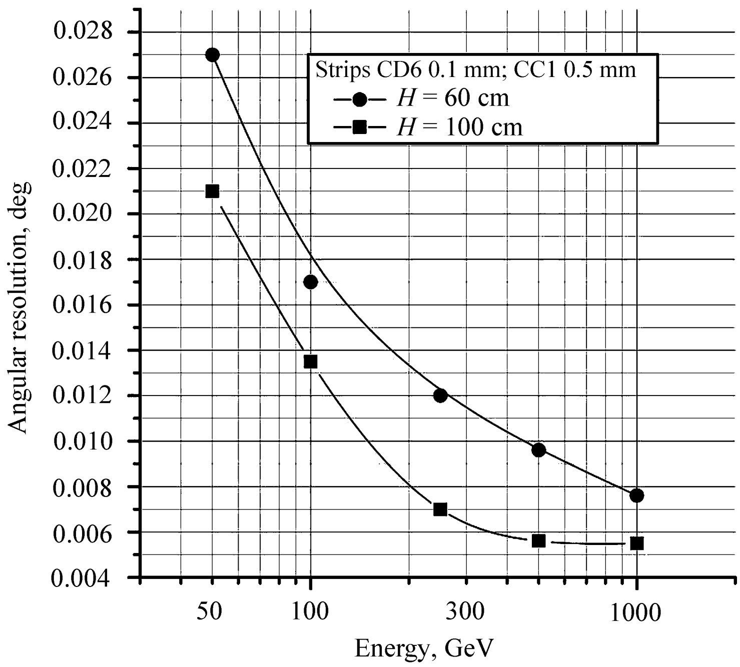

Fig. 6. Energy dependence of the GAMMA-400 angular resolution for various H.

reconstructing the particle arrival direction, based on the technique used in the PAMELA experiment and optimized for new problems, was presented.

ACKNOWLEDGMENTS

This study was performed in the framework of the Federal target program "Scientific and Pedagogical Personnel of Innovative Russia" for 2009–2013.

REFERENCES

1. F. Diego Torres et al., Adv. Space Res. **33**, 450 (2004).
2. M. Basset et al., Nucl. Instrum. Methods Phys. Res. **572**, 474 (2007).
3. John F. Krizmanic et al., Nucl. Instrum. Methods Phys. Res. A **418**, 161 (1998).
4. S. Torii et al., Nucl. Phys. B Proc. Suppl. **166**, 43 (2007).
5. V. Ginzburg et al., Preprint no. 10 (Moscow, LPI, 2009).
6. A. M. Galper et al., Izv. Russ. Akad. Nauk Ser. Fiz. **75**, 471 (2011) [Bull. Ross. Acad. Sci. Phys. **75**, 316 (2011)].
7. A. A. Abdo et al., Astrophys. J. Suppl. **188**, 405 (2010).
8. S. V. Borisov, S. A. Voronov, A. V. Karelin, et al., Pisma Fiz. Elem. Chast. Atom. Yadra, No. 1(157), 68 (2010) [Phys. Part. Nucl. Lett. **7**, 39 (2010)].
9. M. Circella et al., Nucl. Instrum. Methods Phys. Res. A **518**, 153 (2004).
10. S. Agostinelli et al., Nucl. Instrum. Methods Phys. Res. A **506**, 250 (2003).

ISSN 1068-3356, Bulletin of the Lebedev Physics Institute, 2011, Vol. 38, No. 7, pp. 209–214. © Allerton Press, Inc., 2011.
Original Russian Text © A.M. Galper, S.V. Koldashov, and A.A. Ulitin, 2011, published in Kratkie Soobshcheniya po Fizike, 2011, Vol. 38, No. 7, pp. 41–50.

Local Perturbations of the Earth's Radiation Belt during the Seismic Event Development in Japan on March 11, 2011

A. M. Galper[a,b], S. V. Koldashov[b], and A. A. Ulitin[b]

[a] *Lebedev Physical Institute, Russian Academy of Sciences, Leninskii pr. 53, Moscow, 119991 Russia*
[b] *National Research Nuclear University "MEPhI", Kashirskoe sh. 31, Moscow, 115409 Russia*

Received June 21, 2011

Abstract—Energetic electron bursts detected in the ARINA satellite experiment during the development of the catastrophic seismic event in Japan on March 11, 2011 are analyzed. Time profiles of the daily number of particle bursts and earthquakes with magnitudes larger than 4 are compared; synchronous variation of these time profiles is detected.

DOI: 10.3103/S1068335611070025

Keywords: radiation belt, particle precipitation, earthquake prediction.

1. Local perturbations of the radiation belt and particle bursts in the near-Earth space. Within the Federal space program, the ARINA and VSPLESK satellite experiments were prepared and are currently implemented at the MEPhI. These experiments are designed for radiation monitoring of the near-Earth space (NES) with the aim to study the physical nature of energetic charged particle bursts (drastic short-term increases in particle fluxes).

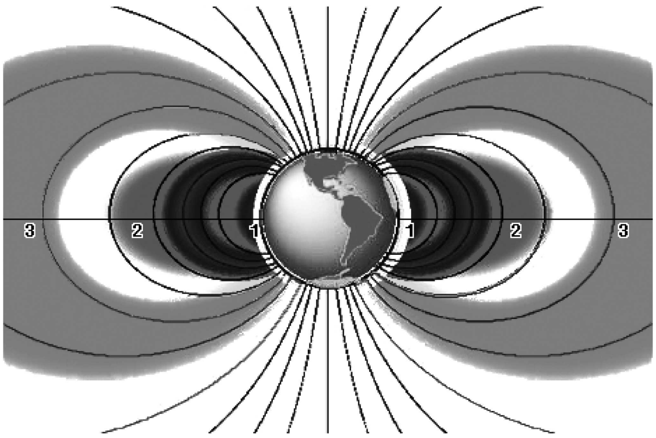

Fig. 1. Meridional section of the Earth's radiation belt: drift shells $L = 1 - 2$ are the inner ERB region and $L = 3 - 7$, outer ERB zone.

The steady-state radiation conditions in the NES are formed by the superposition of galactic cosmic rays, atmospheric albedo particle fluxes, and charged particles trapped by the geomagnetic field (Earth's radiation belt, ERB) [1]. The ERB structure is shown in Fig. 1.

Currently, of great interest are studies of the changes in radiation conditions in the NES outside the ERB region, which appear as bursts and variations of charged particle fluxes in a wide energy range. Energetic particle bursts in the NES were first detected in 1985 in the MARIA experiment performed by the "MEPhI" onboard the Salyut-7 orbiter [2]. Later, extensive experimental and theoretical studies in this field were performed. The correlation between particle bursts and various solar-magnetospheric and

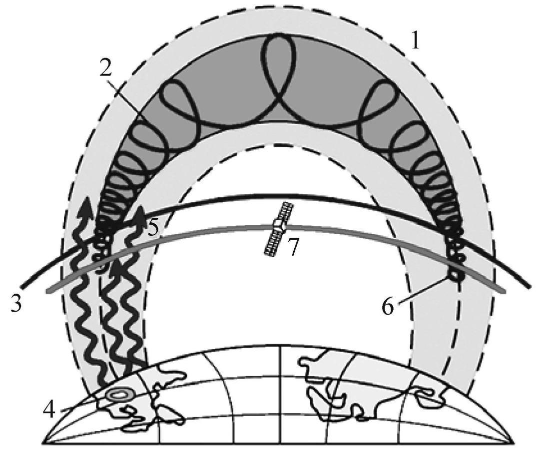

Fig. 2. Precipitation of the radiation belt particles after the interaction with EMR of seismic origin: (1) geomagnetic tube, (2) particle trajectory, (3) lower boundary of the radiation belt, (4) earthquake source, (5) electromagnetic radiation, (6) precipitating particles, and (7) satellite trajectory.

geophysical (seismic, thunderstorm, etc.) processes was established (see [3–12] and references therein). Among the most important experiments are: MARIA, MARIA-2 [4, 5, 7], and SAMPEX/PET [8, 10] at high energies (5–50 MeV); Demeter (0.3–5 MeV) [11] and POES (0.3–2.5 MeV) [12] at low energies.

These studies showed that the formation mechanism of energetic charged particle bursts (observations are mostly related to electrons with energies on the order of several tens of MeV) is associated with local perturbations of the ERB and is as follows [3, 4]. Energetic electrons of the ERB interact with low-frequency electromagnetic radiation (EMR) generated in various geophysical and magnetospheric processes, which results in pitch-angle diffusion of particles and lowering their mirror points. As a result, particles precipitate from the ERB to altitudes below the radiation belt boundary. Figure 2 shows this process in the case of seismic disturbance of the ERB. Then precipitated particles, if their mirror points are not too deep in the residual atmosphere (above 60–80 km), drift around the Earth and form a wave of precipitated particles (referred to as the GKV wave), propagating along the L-shell containing an ERB local perturbation region. The time of the complete longitudinal revolution of energetic particles around the Earth is from several tens of seconds to several minutes. Therefore, for same time, the L-shell is completely filled with precipitated particles. When a spacecraft crosses such a perturbed L-shell, devices record a particle burst which, obviously, can be observed at any longitude not necessarily coinciding with the longitude of the ERB local perturbation region, as well as in the magnetically-coupled zone corresponding to this region. Thus, the NES region, in which particle bursts caused by ERB local perturbations can be detected, significantly broadens and the probability of their detection in spacecraft measurements increases.

In [3, 4], it was shown that geographical coordinates of the ERB local perturbation region, i.e., the position of the region over which particle precipitation occurred (e.g., over the earthquake source, thunderstorm activity area, etc.), can be determined by measuring particle burst characteristics (the detection point, energy spectra, and time profiles). For particle bursts of seismic nature, it was found that they appear several hours before strong earthquakes; currently, approaches to the application of this effect to predict earthquakes are developed [5, 13, 14]. However, the above-mentioned possible difference in the positions of the particle burst observation region in the NES and the ERB local perturbation region creates additional difficulties when identifying the physical nature of the burst.

Therefore, currently, it is important to understand from the practical viewpoint, how measurements of physical characteristics of particle bursts can provide the determination of the burst nature (magnetospheric seismic, lightning, anthropogenic, and others), in particular, the identification of particle bursts associated with earthquakes.

2. Experimental. The ARINA and VSPLESK scintillation spectrometers developed in the MEPhI are fully identical in physical schemes, have identical physical parameters (geometrical factor, energy

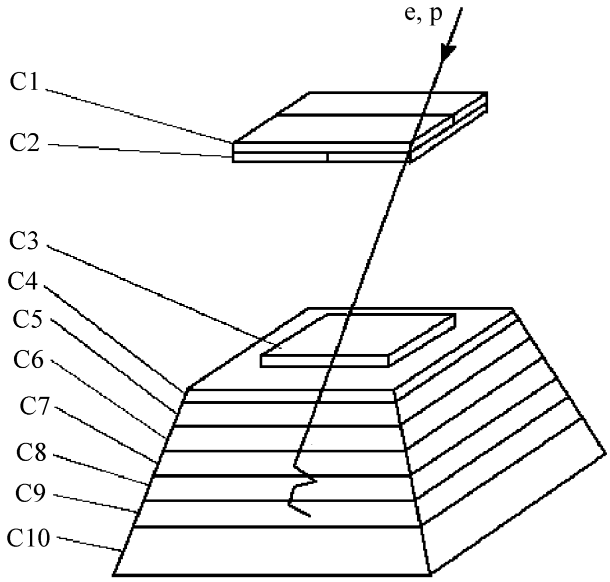

Fig. 3. Physical diagram of the spectrometer.

range, energy resolution, and others), detect and identify electrons (3–30 MeV) and protons (30–100 MeV), measure their energies, and allow the study of energy spectra and time profiles of particle fluxes.

The ARINA and VSPLESK experiments are performed onboard low-orbit spacecrafts. The ARINA device is installed in a hermetic container of the Resurs-DK No. 1 spacecraft with an altitude of 350–600 km and an orbit inclination of 70°; the experiment is performed since the mid-June, 2006 [13].

The VSPLESK device is installed outside the sealed volume on the Service module of the International Space Station (altitude is 350–400 km, an orbit inclination is 52°, measurements are performed since August, 2008) [14].

The matter thickness in the field of view of each spectrometer is $\sim$0.5 g/cm^2. Device axes are perpendicular to spacecraft orbit planes.

Figure 3 shows the physical diagram of the multilayer scintillation detector (MSD) which is a main part of the device.

Charged particles (electrons, protons) moving forward (downward) and arriving at the device aperture sequentially pass through scintillation layers C1, C2, C3, etc., lose energy, and are absorbed in the MSD. Backward particles and particles passed through the entire device are cut by detector C10 operating in the anticoincidence mode. Thus, particles stopped in the MSD are electrons with energies of 3–30 MeV and protons with energies of 30–100 MeV. They are identified by the energy release in each layer when passing through the device and by the range in it. The electron and proton energy is measured by their range in MSD layers. The physical diagram and parameters of the device are described in detail in [15].

The spectrometer makes it possible to measure the energy spectra of particles and to trace their evolution, to determine time profiles of particle bursts with high time resolution, and can operate in high-intensity particle fluxes. The device aperture controlled by the configuration and arrangement of detectors C1–C3 is $\sim$10 cm^{2}sr, which is several tens of times higher than the aperture of the equipment using which the main results on observations of seismic effects in particle fluxes were obtained [8, 10]. The ARINA and VSPLESK characteristics are listed in Table 1. In the present study, we used the experimental data on the total electron flux in the energy range of 3–30 MeV.

3. Experimental results.

3.1. General characteristic of ARINA and VSPLESK experiments. First, it should be emphasized that the measurements performed in the ARINA and VSPLESK experiments are more sensitive to particle flux variations in comparison with previous experiments by more than an order of magnitude [8, 10]. This was achieved due to a significantly larger geometric factor, which allowed separation of

Table 1. Physical and technical characteristics of spectrometers

1.	Geometrical factor		10 cm^{2}sr
2.	Angular aperture		±30°
3.	Energy ranges	for protons for electrons	(30–100) MeV (3–30) MeV
4.	Energy resolution	for protons for electrons	10% 15%
5.	Time resolution		100 ns
6.	Mass		8.6 kg
7.	Power consumption		13.5 W

Fig. 4. Japan region chosen for analysis.

additional weak particle bursts. Almost continuous measurements made it possible to collect statistics on particle bursts, sufficient to perform a statistical analysis and to study the physical nature of particle bursts at the new qualitative level [13, 14, 16].

Bursts of energetic charged particles were detected in each experiment. For further processing and analysis, particle bursts at the level of ∼4.5 standard deviations and above with durations from a few seconds to a few minutes were selected. In total, ∼200 and ∼50 such particle bursts were detected during the ARINA and VSPLESK experiments, respectively.

In [3, 4, 14], the possibilities of remote diagnostics of ERB local perturbations are considered based on the data on characteristics of particle bursts detected in the NES, and examples of detection of seismic

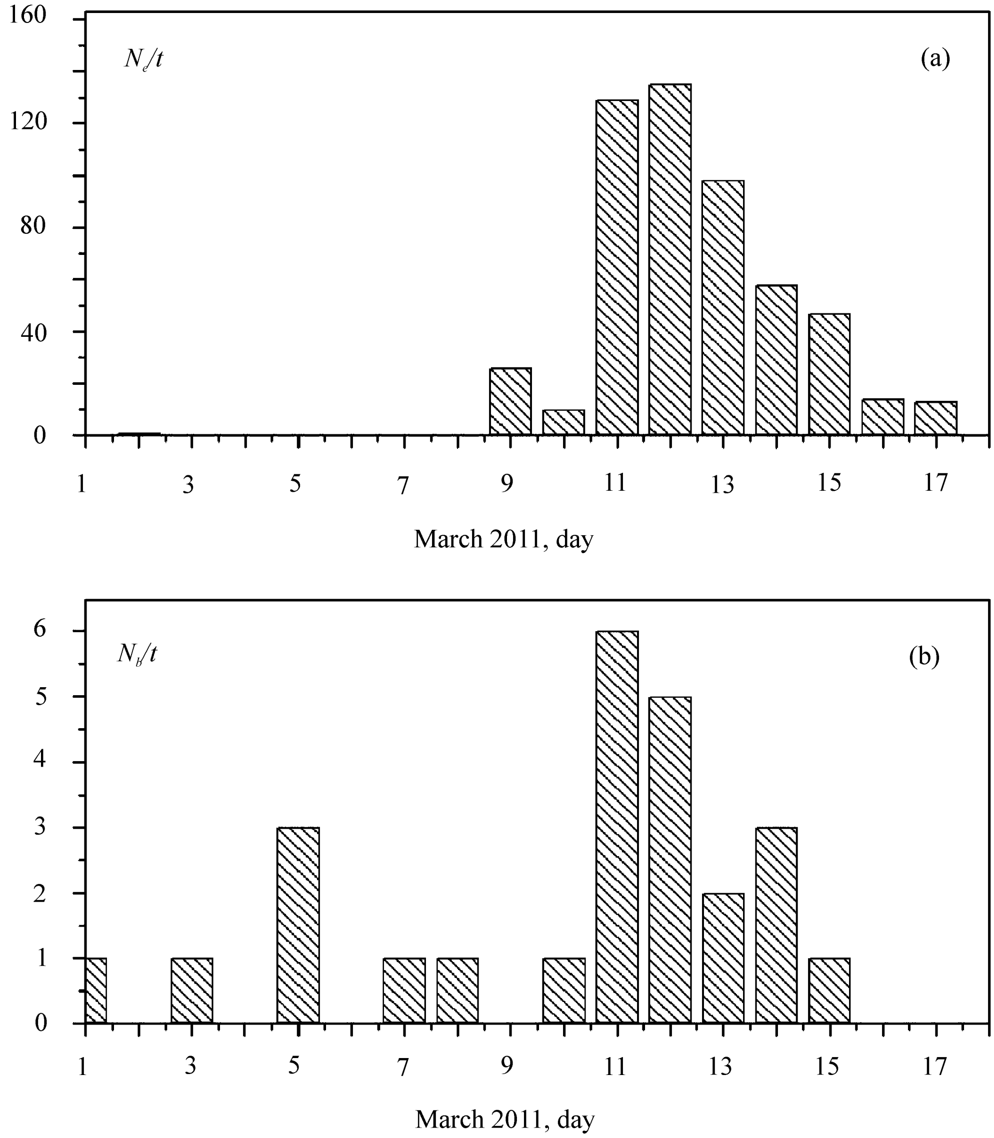

Fig. 5. (a) Number of earthquakes ($M > 4$) and (b) number of particle bursts in the ARINA experiment.

and lightning disturbances of the ERB are given. In [16], particle bursts were detected immediately in ERB local perturbation regions; in particular, it was found that such particle bursts are grouped along tectonic fault lines and over areas of increased thunderstorm activity.

3.2. Particle bursts during the development of the seismic event in Japan on March 11, 2011. The ARINA and VSPLESK experiments are performed in the mode of almost continuous measurements of energetic proton and electron fluxes. Nevertheless, information flow gaps regularly arise in the VSPLESK experiment due to a low speed of the onboard telemetric system, which, in particular, resulted in loss of information relating to the catastrophic seismic event in Japan on March 11, 2011, discussed below. In the ARINA experiment, similar information losses do not exceed 5–10%, and the presented experimental results on this event were obtained by the data on the ARINA experiment.

The strong seismic event in Japan, begun on March 11, 2011 by the earthquake with a magnitude of 9, was accompanied by extraordinarily high aftershock activity with a number of earthquakes (with magnitudes $M > 4$) to 140 a day. Thus, in this case, the previously used analysis method [8] based on separation of two genetically related events (particle burst and earthquake) and designed for relatively rare events (less than ten a day) cannot be used. Nevertheless, it should be noted that in the region geomagnetically coupled with the seismically active region in Japan, at 03:42:27 UT, a particle burst (at the level of 3.2 standard deviations) was detected, which could probably be a precursor of the first main earthquake ($M = 9$) occurred at 05:46:23 UT.

As applied to the entire seismic event, the following approach to the analysis of bursts of energetic charged particles was used. A Japan region was selected with geographical coordinates of 140–155° longitude and 33–45° latitude (Fig. 4). Then in this region (in the NES over it), the time profile of the counting rate N_b/t of particle bursts (the number of bursts a day) in the time interval before the seismic event and during its development was determined. Then in the same time interval, N_b/t were compared to the behavior of the daily number of earthquakes (N_e/t) with magnitudes above a set one (e.g., of magnitude 4 by the Richter scale; the ANSS catalog was used: http://www.ncedc.org/anss/catalog-search.html).

The behavior of N_b/t and N_e/t from March 1 to March 16 is shown in Figs. 5(a) and 5(b). We can see a sharp severalfold increase in the number of particle bursts since March 11, 2011, which correlates with the sharply increased number of earthquakes in the chosen region. However, it should be taken into account that observation of particle bursts in a certain region from a single spacecraft is strongly time-limited, since a spacecraft crosses this region no more than several times a day, and the crossing time is about several minutes. At the same time, seismic events are observed by ground-based geophysical services continuously. Therefore, the number of detected earthquakes significantly exceeds the number of detected particle bursts.

Conclusions. The presented results of observations of the dynamics of energetic electron fluxes in the NES during the development of the seismic event in Japan on March 11, 2011 are an example of the seismomagnetospheric relation and demonstrate the applicability of this phenomenon to satellite monitoring of earthquakes.

REFERENCES

1. J. G. Roederer, *Dynamics of Geomagnetically Trapped Radiation* (Springer, Berlin, 1970; Mir, Moscow, 1972).
2. S. A. Voronov, A. M. Galper, V. G. Kirillov-Ugryumov, et al., in: *Proceedings of the 20th International Cosmic Ray Conference, Moscow, Russia, 1987* (Nauka, Moscow, 1997), Vol. 4, p. 451.
3. A. M. Galper, S. V. Koldashov, and A. M. Murashov, Kosm. Issled. **38**, 102 (2000) [Cosmic Research **38**, 96 (2000)].
4. M. E. Aleshin, S. A. Voronov, A. M. Galper, et al., Kosm. Issled. **30**, 79 (1992).
5. A. M. Galper, S. V. Koldashov, and S. A. Voronov, Adv. Space Res. **15**(11), 131 (1995).
6. S. Yu. Aleksandrin, S. A. Voronov, A. M. Galper, et al., Izv. Ross. Akad. Nauk Ser. Fiz. **65**, 400 (2001).
7. S. Yu. Aleksandrin, S. A. Voronov, A. M. Galper, et al., Izv. Ross. Akad. Nauk Ser. Fiz. **67**, 79 (2003).
8. S. Yu. Aleksandrin, A. M. Galper, S. V. Koldashov, et al., Ann. Geophys. **21**, 597 (2003).
9. S. Yu. Aleksandrin, A. M. Galper, S. V. Koldashov, and A. M. Murashov, Izv. Ross. Akad. Nauk Ser. Fiz. **69**, 872 (2005).
10. V. Sgrigna, L. Carota, L. Conti, et al., J. Atm. Solar-Terr. Phys. **67**, 1448 (2005).
11. M. Parrot, J. J. Berthelier, J. P. Lebreton, et al., Phys. Chem. Earth **31**, 486 (2006).
12. C. Fidani, R. Battiston, and W. J. Burger, Remote Sensing, **2**, 2170 (2010).
13. A. V. Bakaldin, A. G. Batishchev, S. A. Voronov, et al., Kosm. Issled. **45**, 471 (2007) [Cosmic Research **45**, 445 (2007)].
14. S. Yu. Aleksandrin, A. V. Bakaldin, A. G. Batishchev, et al., Izv. Ross. Akad. Nauk Ser. Fiz. **73**, 379 (2009) [Bull. Russ. Acad. Sci. Phys. **73**, 361 (2009)].
15. A. G. Batishchev, S. A. Voronov, S. V. Koldashov, et al., Prib. Tekh. Eksp., No. 5, 25 (1999) [Instrum. Exp. Tech. **42**, 604 (1999)].
16. S. Yu. Aleksandrin, A. M. Galper, S. V. Koldashov, et al., in: *Proceedings of the 31st International Cosmic Ray Conference, Moscow, Russia, 2010* (MGU, Moscow, 2010), GEO_9; http://cr2010.sinp.msu.ru/papers/geo_09.pdf.